

Imaging of the umbrella motion and tunneling in ammonia molecules by strong-field ionization

Johann Förster, Etienne Plésiat,* Álvaro Magaña, and Alejandro Saenz

AG Moderne Optik, Institut für Physik, Humboldt-Universität zu Berlin, Newtonstrasse 15, D-12489 Berlin, Germany

(Received 25 July 2016; published 5 October 2016)

The geometry-dependent ionization behavior of ammonia molecules is investigated. Different theoretical approaches for obtaining the ionization yield are compared, all of them showing a strong dependence of the ionization yield on the inversion coordinate at long wavelengths (≥ 800 nm). It is shown how this effect can be exploited to create and probe nuclear wave packets in neutral ammonia using *Lochfraß*. Furthermore, imaging of a wave packet tunneling through the barrier of a double-well potential in real time is discussed.

DOI: [10.1103/PhysRevA.94.043405](https://doi.org/10.1103/PhysRevA.94.043405)**I. INTRODUCTION**

The intense, ultrashort laser pulses that became accessible during the last decade offer prospects to manipulate and image molecules on their natural scales (subfemtosecond and subangstrom). Investigating the response of small molecules to these laser fields, especially high-harmonic generation (HHG) and ionization (seen as the first step of HHG), led to the development of promising concepts to produce a real-time movie of the electronic and nuclear dynamics triggered in these molecules. The information contained in high-harmonic radiation emitted from these molecules may be used for, e.g., orbital tomography [1], probing of nuclear dynamics with subfemtosecond resolution [2–6], and imaging coupled electron-nuclear dynamics [7,8]. Furthermore, the electrons emitted by ionization contain structural information suitable for orbital imaging [9,10]. Since nuclear motion may strongly influence the ionization behavior, these electrons also contain information about the nuclear dynamics, as discussed in the following.

For the example of molecular hydrogen it was found experimentally that the transition from the neutral molecule to the molecular ion may not follow the Franck-Condon distribution [11]. This experiment confirmed an earlier prediction [12] in which the effect was explained assuming a much faster response of the electrons to a laser field compared to the response of the nuclei. Consequently, a vertical electronic transition occurs at fixed nuclear geometries. The breakdown of the Franck-Condon approximation stems from the exponential dependence of the strong-field ionization rates on the binding energy of the ejected electron [13–15] (ionization potential of the initial state). Already, small changes in the binding energy lead to a very pronounced dependence of the electronic transition amplitude on nuclear geometry [12]. This is the case when the equilibrium geometry of the initial state of the neutral molecule and the final state of the molecular ion are significantly different. This prediction of a possibly strong internuclear-separation-dependent ionization probability was later further confirmed by explicit solutions of the time-dependent Schrödinger equation of H_2 [16–18]. A process termed *Lochfraß* [19] was theoretically proposed as a method which exploits the extreme nuclear geometry

dependence of strong-field ionization rates to create and measure nuclear wave packets in the electronic initial states of neutral molecules. Indeed, *Lochfraß* was found to be the dominant mechanism (compared to bond softening) in experiments imaging a vibrational wave packet in neutral diatomic molecules with subfemtosecond and subangstrom resolution [20–22]. Remarkably, it was possible to follow the nuclear wave packet experimentally for an extremely long time window (larger than 1 ps) [20], leading to the proposal of a molecular clock. Furthermore, this mechanism was shown to orient polar molecules due to the rotational wave packet created by orientation-dependent ionization [23,24].

The ammonia molecule undergoes a significant equilibrium geometry change (pyramidal to plane) upon ionization and is thus a good candidate for observing *Lochfraß* in a molecule beyond diatomics. Recently, the relative nuclear motion launched in the cations NH_3^+ and ND_3^+ was studied and experimentally observed by comparison of the respective high-harmonic spectra [5,6] using the so-called probing attosecond dynamics with chirp-encoded recollisions (PACER) technique [2,3]. It was shown that the required nuclear autocorrelation functions can be obtained from photoelectron spectra [4–6]. The photoelectron spectra revealed that the inversion (or umbrella) mode is the only vibrational mode in which a significant nuclear motion is triggered by the laser field [5]. Importantly, it was shown that the strong geometry dependence of the ionization rate, the key ingredient for *Lochfraß*, must indeed be considered in order to quantitatively match the experimental PACER results [5,6].

In the following section we briefly discuss the methods and basis-set parameters used to describe the electronic response (ionization) and triggered nuclear motion in neutral ammonia. In Sec. III we discuss the observed ionization behavior and its application to imaging based on *Lochfraß*. Section IV introduces the idea to image a tunneling wave packet. This idea is further fleshed out in Sec. V, where the observation of the tunneling process in real time and the required laser fields and ionization behavior to achieve this goal are discussed.

II. METHODS

In order to study nuclear motion in neutral ammonia, we first describe the geometry-dependent electronic response (ionization) of the molecule to the laser field. Thereafter, this response is included in the description of the (slower)

*Present address: CIC nanoGUNE, Tolosa Hiribidea, 76, E-20018 Donostia, San Sebastián, Spain.

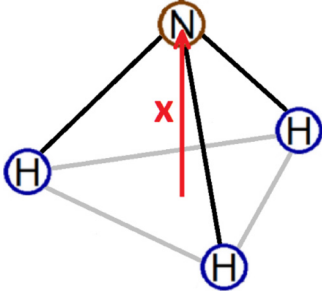


FIG. 1. Geometry of the NH_3 molecule. The inversion coordinate x (red arrow) describes the distance of the nitrogen atom from the center of the triangle spanned by the three hydrogen atoms (for a negative x the nitrogen atom is located below the triangle).

nuclear motion. Unless noted otherwise, atomic units with $\hbar = e = m_e = 4\pi\epsilon_0 = 1$ are adopted.

The time-dependent Schrödinger equation (TDSE) describing the electronic response for a fixed nuclear geometry is solved using the single-determinant approach, which has been described in detail in our previous works [4,10,25,26]. Briefly, a multicenter B -spline approach is used to solve the Kohn-Sham Hamiltonian. The ground-state density calculated from a density-functional-theory calculation employing the ADF quantum chemistry software [27] is employed to construct the Kohn-Sham Hamiltonian, which is then fully diagonalized in a multicentric B -spline basis. We then time propagate in the basis of these orbitals without freezing any of the lower-lying states in the expansion. In the case considered here in which ionization from the $3a_1$ highest occupied molecular orbital (HOMO) dominates the ionization yield, the total yield is calculated as the sum over the individual populations $P_j = |c_j|^2$ of the continuum orbitals (with energy $E \geq E_{\text{thr}}$) after the laser field,

$$Y = \sum_{j; E_j \geq E_{\text{thr}}} P_j. \quad (1)$$

In order to describe the inversion (or umbrella) motion of ammonia, the main nuclear coordinate considered here is the inversion coordinate x (see Fig. 1). We calculate the electronic basis for different values of this inversion coordinate using exactly the same nuclear geometries as in Table 1 of Ref. [28]. A box size of 300 a.u. and a central expansion of 449 B -spline functions (times a spherical harmonic) are used. The maximum angular momentum included is $l_{\text{max}} = 11$. In order to check the convergence of the results, we performed a reference calculation with a larger box of size 600 a.u., 776 B -spline functions, and maximum angular momentum $l = 8$. With this basis, we checked the ionization yields for three different geometries, namely, $x = 0, 0.592$, and 1.066 a.u., and found no deviations from the results obtained with the smaller box size on the level of the graphs shown in the following.

The linearly polarized laser field is described classically by the vector potential

$$\vec{A}(t) = \begin{cases} \vec{A}_0 \cos^2(\pi t/T) \sin(\omega t + \varphi) & \text{for } |t| \leq T/2, \\ 0 & \text{elsewhere,} \end{cases} \quad (2)$$

with laser frequency $\omega = 2\pi c/\lambda$ (wavelength λ , speed of light c), carrier-envelope phase φ , and total pulse duration

$T = 2\pi n_c/\omega$ (number of cycles n_c). In the following $\varphi = 0$ is used. The interaction potential reads $\hat{V}(t) = \hat{\mathbf{p}} \cdot \vec{A}(t)$ (dipole approximation, velocity gauge). The polarization vector \vec{A}_0 points along the inversion axis (and thus the static dipole moment) of ammonia. Ionization from the $3a_1$ HOMO orbital is geometrically preferred for this orientation. This orientation has already been experimentally realized, and variation of the orientation did not reveal contributions to the ionization from lower-lying orbitals [5].

The TDSE ionization yields are compared to the ones obtained using Ammosov-Delone-Krainov (ADK) tunneling rates Γ_{ADK} [14,15] and the recently introduced frequency-corrected ADK (FC-ADK) model [18] based on the Perelomov-Popov-Terent'ev (PPT) [13] theory. By integrating the tunneling rate over the whole pulse duration, one obtains the ionization yield

$$Y(x) = 1 - \exp \left\{ - \int \Gamma[F_e(t), I_p(x)] dt \right\}, \quad (3)$$

where $F_e(t)$ is the envelope function of the electric field and $I_p(x)$ is the vertical binding energy. For consistency, we use the same geometry-dependent $I_p(x)$ as in the TDSE calculations (from the diagonalization of the Kohn-Sham Hamiltonian in the B -spline basis). The FC-ADK ionization rate is defined as [18]

$$\Gamma_{\text{FC-ADK}} = N_e \sqrt{\frac{3F_e}{\pi\kappa^3}}^{2/\kappa - 1} \frac{F_e}{8\pi} \left(\frac{4e\kappa^3}{(2/\kappa - 1)F_e} \right)^{2/\kappa} \times \exp \left[- \frac{2\kappa^3}{3F_e} g(\gamma) \right], \quad (4)$$

where $e = 2.718\dots$, $\kappa = \sqrt{2I_p(R)}$, $\gamma = \kappa\omega/F_e$, and N_e is the number of active electrons. FC-ADK differs from ADK by only the function $g(\gamma)$ [13],

$$g(\gamma) = \frac{3}{2\gamma} \left\{ \left(1 + \frac{1}{2\gamma^2} \right) \text{arcsinh}\gamma - \frac{\sqrt{1+\gamma^2}}{2\gamma} \right\} \quad (5)$$

[in the limit $\gamma \ll 1$, $g(\gamma)$ approaches 1, and thus, FC-ADK becomes identical to standard ADK].

Since the magnetic-field component of the laser field is neglected in this work, the electrons occupying the same spatial orbital (but possessing different spins) respond to the laser field in an identical fashion and are thus equivalent. In the case of neutral ammonia this leads to $N_e = 2$ for the two electrons initially occupying the HOMO. However, the ionization in intense laser fields depends exponentially on the ionization potential. If the intensity and duration of the laser pulse lead to pronounced ionization, the initial electron density is substantially depleted. This results in an increased ionization potential and thus a decreased ionization probability. Therefore, the ionizations from different orbitals are no longer independent of each other. For example, if effectively one electron has been ejected, the ionization of a second (in the single-particle approximation formally independent) electron from the same spatial orbital depends not on the ionization potential of the neutral molecule but on the higher one of the molecular cation. For the H_2 molecule it was confirmed in [25] that the single-active-electron ionization yield matches the full two-electron solution if it is multiplied by a factor 2

($N_e = 2$ active electrons) as long as the ionization yield is small. However, for ion yields $Y \approx 0.1$ a sharp transition was found, and for higher yields the two-electron calculation agreed well with the single-active-electron result if $N_e = 1$ was used. Assuming a comparable behavior for ammonia, i.e., that $N_e = 2$ is appropriate for ion yields below about 10 %, all ion yields obtained within the present TDSE approach and (FC-)ADK for intensities lower than $I = 10^{14}$ W/cm² adopt $N_e = 2$ ($N_e = 1$ otherwise).

If a significant part of the initial nuclear wave function gets ionized, as is the case for *Lochfraß*, the effect of the ionization process on the nuclear motion in the electronic ground state of the neutral molecule is incorporated by means of a loss channel (ignoring a possible recombination) [19]. This leads to the one-dimensional time-dependent Schrödinger equation for the inversion coordinate x ,

$$i \frac{\partial}{\partial t} \chi(x, t) = \left(\hat{H}_0 - \frac{i\Gamma(x, t)}{2} \right) \chi(x, t), \quad (6)$$

where \hat{H}_0 is the time-independent nuclear Hamiltonian and $\Gamma(x, t)$ is the geometry-dependent ionization rate. In the limit of an extremely fast ionization process compared to the time scale of nuclear motion (instantaneous ionization and vertical transition), an initial nuclear wave function $\chi_0(x)$ is transformed into

$$\sqrt{1 - Y(x)} \chi_0(x). \quad (7)$$

In the following, this limit is termed the sudden-ionization approximation. To obtain an ionization rate $\Gamma_{\text{TDSE}}(x, t)$ for the electronic TDSE calculations, we assume the time dependence of FC-ADK and scale the rate with a constant factor $q(x)$, $\Gamma_{\text{TDSE}}(x, t) = q(x) \Gamma_{\text{FC-ADK}}(x, t)$. This is done such that the integration of $\Gamma_{\text{TDSE}}(x, t)$ according to Eq. (3) gives the correct ionization yield $Y_{\text{TDSE}}(x)$.

For the time-independent umbrella motion, we follow the approach in Ref. [28] and adopt the position-dependent mass Hamiltonian [29]

$$\hat{H}_0 = \frac{1}{2} \hat{p} \frac{1}{\mu(x)} \hat{p} + V(x), \quad (8)$$

where $V(x)$ is the double-well potential from Table 1 of Ref. [28] and

$$\mu(x) = \frac{3m_{\text{H}}m_{\text{N}}}{3m_{\text{H}} + m_{\text{N}}} + \frac{3m_{\text{H}}x^2}{r_0^2 - x^2} \quad (9)$$

is the position-dependent mass, where $r_0 = 1.0041$ a.u. and m_{H} (m_{N}) denotes the mass of the hydrogen (nitrogen) atom. The position-dependent mass effectively includes the change in the size of the triangle spanned by the three hydrogen atoms during the umbrella motion (variation of x). Remarkably, the energies of the eight lowest-lying vibrational states differ by at most 5.6% from their experimental values, compared to 32.4% if one would adapt a constant mass instead [28,30]. Equation (8) and its solution have been discussed in detail in [30]. For the solution of Eqs. (8) and (6) using the method described in [30] (and its time-dependent formulation using fast-Fourier transformations), we use a box size of $x_{\text{max}} = \pm 1.805$ a.u. and $N = 71$ points (converged results are obtained already with $N = 31$ points).

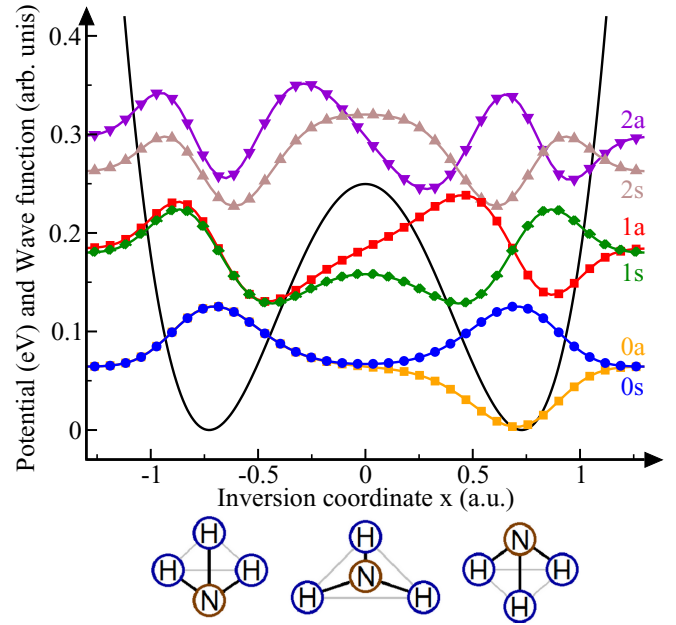


FIG. 2. Electronic ground-state potential of NH₃ (solid black line) and vibrational eigenfunctions (solid colored lines with symbols) labeled by symmetry (s, symmetric, or a, antisymmetric) with respect to a reflection at $x = 0$. The eigenfunctions are vertically shifted such that they approach their respective eigenenergies in the limit $|x| \rightarrow \infty$.

Figure 2 shows the six lowest-lying vibrational eigenfunctions of NH₃ obtained with the present method. The energy splitting between the first two vibrational (inversion) eigenstates is extremely small (≈ 0.8 cm⁻¹ [28,30,31]). Thus, if the ammonia molecule is initially in thermal equilibrium, the initial state is (as also discussed in [6]) a thermal mixture consisting of 50% in the lowest symmetric state $|0s\rangle$ and 50% in the lowest antisymmetric state $|0a\rangle$ for a large temperature regime (4 K $< T < 300$ K). This requires a density-matrix formulation for the evolution of the vibrational wave packet. The solution simplifies, however, if the inversion symmetry is not broken at any time, $\Gamma(x, t) = \Gamma(-x, t)$. In this case, one can numerically solve the Schrödinger equation (6) independently for $|0s\rangle$ or $|0a\rangle$ as the initial state, instead of propagating the whole density matrix.

III. IONIZATION BEHAVIOR AND APPLICATION TO IMAGING (*LOCHFRASS*)

The ionization yields obtained from the solution of the TDSE as well as from the ADK and FC-ADK rates are shown in Fig. 3 for $n_c = 6-10$ cycle pulses and wavelengths of $\lambda = 800, 1300,$ and 1800 nm. The TDSE ionization yields are almost perfectly symmetric with respect to the inversion coordinate x ; that is, the ionization yield is unchanged whether the maximum of the electric field is oriented parallel or antiparallel to the inversion axis (see Fig. 4). While ADK qualitatively predicts the correct geometry dependence of the ionization yield, FC-ADK also agrees quantitatively very well with the TDSE results over the whole intensity range, similar to observations for the H₂ molecule [18]. The largest

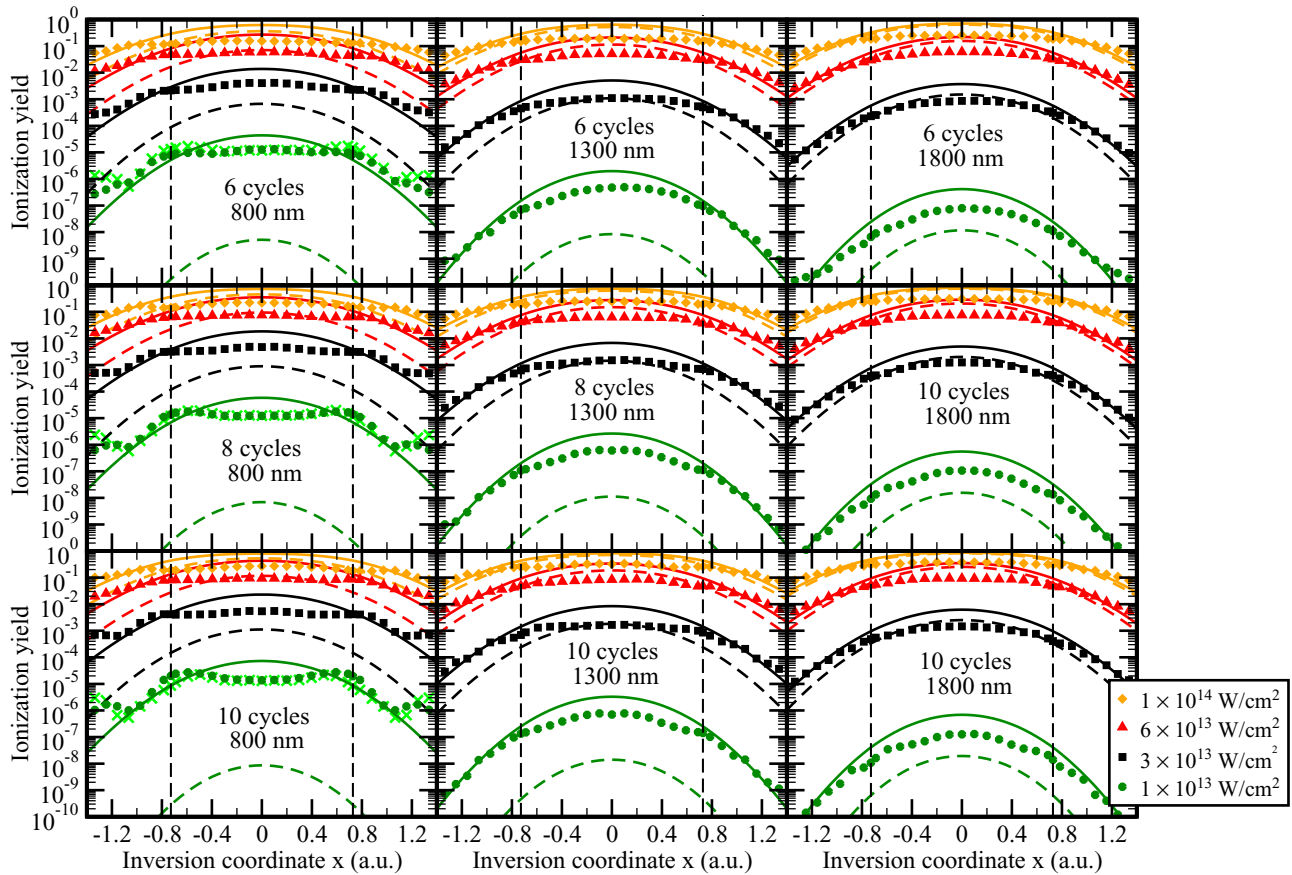


FIG. 3. Geometry-dependent ionization yields obtained from TDSE (points), ADK (dashed lines), and FC-ADK (solid lines) for different intensities, wavelengths, and numbers of laser cycles (values are given inside the graph). The dashed vertical lines indicate the equilibrium geometry at $x_{eq} = \pm 0.728$ a.u. Furthermore, the light green crosses display the excitation yield for $\lambda = 800$ nm and peak intensity 10^{13} W/cm².

differences between ADK and FC-ADK are observable at low intensities and $\lambda = 800$ nm. The differences between ADK and FC-ADK decrease with increasing wavelength and intensity due to the decreasing Keldysh parameter. Furthermore, one can observe how the TDSE ionization yields also become

smoother for decreasing Keldysh parameters; that is, multiphoton resonances get less important when going deeper into the quasistatic regime. Except for a seemingly reduced ionization yield around $x = 0$ for the TDSE at $\lambda = 800$ nm and $I = 10^{13}$ W/cm², all predictions show a significant increase in the ionization yield with decreasing absolute value of the inversion coordinate $|x|$. This is expected due to the decrease in the vertical binding energy $I_p(x)$ with decreasing $|x|$ which stems from the change in the equilibrium geometry from pyramidal to planar upon ionization (see also Fig. 5). The exponential dependence of the ionization rate on the binding energy, Eq. (4), leads to this increase. However, the TDSE shows a less pronounced $|x|$ dependence than ADK and FC-ADK. Especially at small $|x|$, the TDSE ionization yield behaves much flatter than in the (FC-)ADK case.

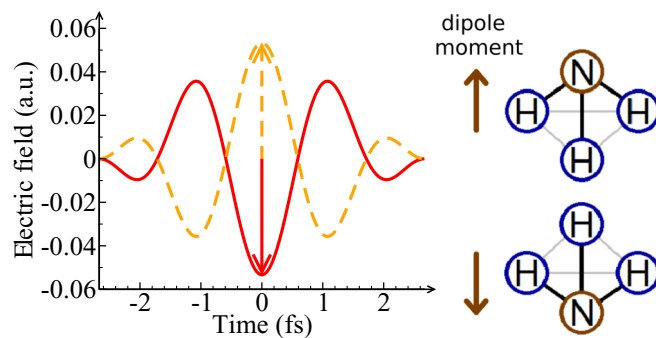


FIG. 4. The time dependence of an electric field with $n_c = 2$ cycles total duration, wavelength $\lambda = 800$ nm, peak intensity $I = 10^{14}$ W/cm², and carrier-envelope phase $\varphi = 0$ ($\varphi = \pi$) is shown on the left as a dashed orange (solid red) line. For an electric field pointing along the inversion axis going through the nitrogen atom and the center of the triangle spanned by the hydrogen atoms, the maximum of the field may point parallel or antiparallel to the dipole moment of the molecule, as indicated on the right.

In order to understand the already mentioned seemingly reduced ionization yield around $x = 0$ found for $\lambda = 800$ nm (especially, for $I = 10^{13}$ W/cm²), it has to be noted again that these parameters indicate that the picture of multiphoton ionization becomes increasingly more adequate to describe the ionization behavior since one finds, for the Keldysh parameter, $\gamma \approx 3$. One prominent signature of multiphoton ionization is the occurrence of resonance-enhanced multiphoton ionization (REMPI). As a more detailed analysis reveals, there is no suppression of the ionization yield around $x = 0$, but an increase of the ionization yield can be observed due to

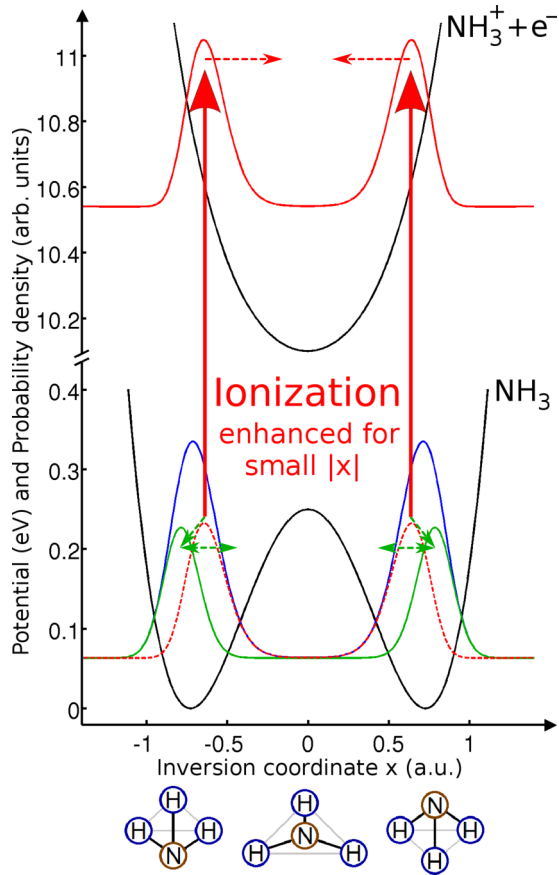


FIG. 5. Potential-energy curves of the electronic ground states of NH_3 and NH_3^+ (black lines) and probability density of the initial state (blue line). The solid red line indicates the density generated in NH_3^+ due to ionization. This part of the probability density is then missing in neutral NH_3 , as indicated by the dashed red line, such that the density indicated by the green line is created.

REMPI processes at $x \approx \pm 0.7$ a.u. and $x \approx \pm 1.3$ a.u. These maxima are responsible for the local minimum at $x = 0$. This explanation is validated by considering the excitation yield (population of all initially unoccupied orbitals with energy below the ionization threshold) that is also shown (for three laser pulses) in Fig. 3. The excitation yield behaves similarly to the ionization yield and is quantitatively comparable to or, for $n_c = 6$ cycles, even exceeds the ionization yield, confirming the occurrence of REMPI processes. Furthermore, with increasing pulse duration, resonance structures become narrower and more pronounced due to the narrower frequency bandwidth of the Fourier-limited laser pulse. This is in agreement with the pulse-length dependence of the structures seen in both the ionization and excitation yields. The maxima (and thus also the local minimum at $x = 0$) are most prominent for the longest pulses considered in this work. Since REMPI processes are by definition not considered in ADK and FC-ADK, the seeming agreement of FC-ADK with the TDSE results around $|x| = 0.7$ a.u. is thus, in fact, accidental and due to an overall overestimation of the ion yield within FC-ADK at those laser parameters.

We now consider *Lochfraß* as in previous studies for diatomic molecules [19–22]. Starting from ammonia in its

thermal equilibrium state (50% $|0s\rangle$ and 50% $|0a\rangle$), the geometry dependence of the ionization yield will create a wave packet as sketched in Fig. 5. The wave packet created in the NH_3^+ ion (Fig. 5, top) is shifted towards smaller values of $|x|$ due to the enhancement of the ionization yield at smaller $|x|$. This wave packet will then move towards the potential minimum of NH_3^+ (see [6] for a detailed study). Since the probability density remaining in neutral NH_3 is mostly depleted at small values of $|x|$, a wave packet shifted towards larger values of $|x|$ remains after ionization (Fig. 5, bottom). This wave packet will then oscillate inside the minima of the double-minimum potential. To probe the wave packet in neutral NH_3 , one can again exploit the geometry dependence of the ionization yield. Whenever the wave packet is close to the potential barrier around $x = 0$ a.u., the total ionization probability will be enhanced compared to positions farther away from the barrier. Thus, one can use a pump pulse to create the wave packet and image it with a probe pulse. The created wave packet can then be followed in real time by varying the pump-probe delay. Figure 6 shows the ionization yield of the probe pulse as a function of the pump-probe delay using two delayed, identical $n_c = 10$ cycle pulses with a peak intensity of $I = 10^{14}$ W/cm² and wavelengths $\lambda = 800, 1300,$ and 1800 nm. In all cases a similar oscillation of the ionization yield is observed. This oscillation can easily be understood considering that the symmetry with respect to x is not broken at any time and that the probability densities of $|0s\rangle$ and $|0a\rangle$ are (almost) equal. Thus, two independent oscillations with initially the same amplitude and phase are launched, one for the symmetric part and another one for the antisymmetric part. Like for H_2 [19], mainly the first excited state (but here of each symmetry) gets populated by the pump pulse. The oscillations for each symmetry have a period of

$$T_s = \frac{2\pi\hbar}{E_{1s} - E_{0s}} \approx 35.80 \text{ fs}, \quad (10)$$

$$T_a = \frac{2\pi\hbar}{E_{1a} - E_{0a}} \approx 34.47 \text{ fs}. \quad (11)$$

Due to this slight difference in their oscillation periods (or frequencies), both contributions will cancel out after

$$\frac{T_{\text{envelope}}}{2} = \frac{T_s T_a}{2(T_s - T_a)} \approx 462 \text{ fs} \quad (12)$$

and will revive after T_{envelope} , as seen in Fig. 6 for all cases. Regarding the absolute numbers, one can see that ADK and FC-ADK predict a significantly larger contrast (oscillation height vs average value of the ionization yield) than the TDSE. This is due to the much smaller $|x|$ dependence of the TDSE ionization yields for $I = 10^{14}$ W/cm² (see Fig. 3). Especially for 800 nm, the contrast $C = (Y_{\text{max}} - Y_{\text{min}})/Y_{\text{average}}$ is extremely small in the TDSE case, $C_{\text{TDSE}} \approx 0.0023$ compared to $C_{\text{ADK}} \approx 0.072$ and $C_{\text{FC-ADK}} \approx 0.10$. For 1800 nm, the contrast changes mainly for the TDSE and is larger, $C_{\text{TDSE}} \approx 0.0053$, but still more than an order of magnitude smaller than $C_{\text{FC-ADK}} \approx 0.078$. Even longer wavelengths could possibly improve the contrast further. The sudden-ionization approximation for the nuclear motion, Eq. (7), which is also shown in Fig. 6, agrees qualitatively very well (almost quantitatively) with the time-dependent solution of Eq. (6). It is noteworthy that for the TDSE results

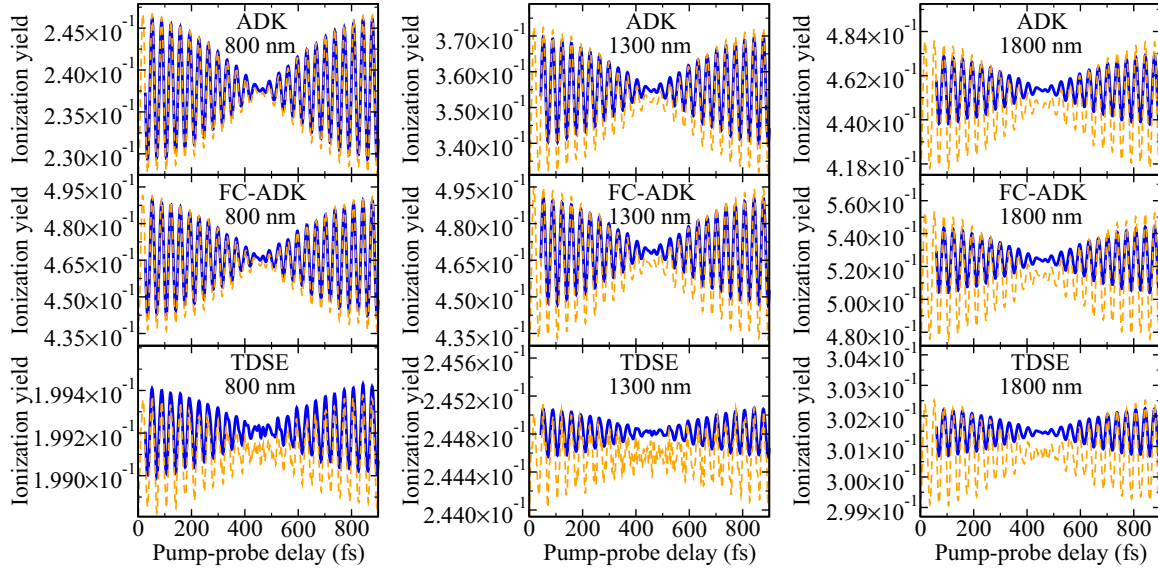


FIG. 6. Probe-pulse ionization yield as a function of the pump-probe delay. A ten-cycle 10^{14} W/cm 2 pump pulse is followed by an identical ten-cycle 10^{14} W/cm 2 probe pulse. Shown is the full time-dependent solution of Eq. (6) (solid blue lines) and the sudden ionization approximation, Eq. (7) (dashed orange lines).

at 800 and 1300 nm, where the signal is very small, the sudden ionization approximation shows a “spikier” signal.

Figure 7 considers a similar pump-probe scheme as before, but with a lower probe-pulse intensity of $I = 4 \times 10^{13}$ W/cm 2 . Since the geometry dependence of the TDSE ionization yield is larger for smaller intensities, one would expect a higher contrast. Indeed, the contrast now reaches the percentage regime, namely, $C_{\text{TDSE}} \approx 0.007$ (0.01, 0.02) for 800 (1300, 1800) nm. The contrast may be further increased using even lower probe-pulse intensities. This would lead to even lower total ionization yields, which, however, may cause practical problems due to experimental sensitivity limits. The optimal intensity is thus a

compromise between contrast and sensitivity and depends on the given experimental setup.

IV. IMAGING OF A TUNNELING WAVE PACKET

Since the ionization yield gets larger whenever a wave packet moves closer to the barrier of the double-well potential, one may think to exploit this behavior to directly observe a wave packet tunneling through the barrier. Considering a coherent superposition of the two lowest vibrational eigenstates,

$$|\chi(t=0)\rangle = \frac{1}{\sqrt{2}}(|0s\rangle + |0a\rangle), \quad (13)$$

a wave packet tunneling from one side to the other is achieved. This wave packet can be realized considering that the ammonia maser operates on the $|0s\rangle \leftrightarrow |0a\rangle$ transition [32]. Starting from a beam of $|0a\rangle$ states within a maser setup, the wave packet $|\chi(t=0)\rangle$ is created after a quarter of the maser transition period and may then propagate freely. Then, after

$$\tau = \frac{\pi \hbar}{E_{0a} - E_{0s}} \approx 20 \text{ ps}, \quad (14)$$

this wave packet will have tunneled completely to the other side. The probability density $\rho(x, t) = |\chi(x, t)|^2$ of the wave packet evolves according to

$$\rho(x, t) = \cos^2\left(\frac{\pi t}{2\tau}\right) \rho_{\text{left}}(x) + \sin^2\left(\frac{\pi t}{2\tau}\right) \rho_{\text{right}}(x), \quad (15)$$

where

$$\rho_{\text{left}}(x) = \rho(x, 0) = \frac{1}{2} |\Psi_{0s}(x) + \Psi_{0a}(x)|^2 \quad (16)$$

corresponds to the probability density localized on the left side of the double-well potential and

$$\rho_{\text{right}}(x) = \rho(x, \tau) = \frac{1}{2} |\Psi_{0s}(x) - \Psi_{0a}(x)|^2 \quad (17)$$

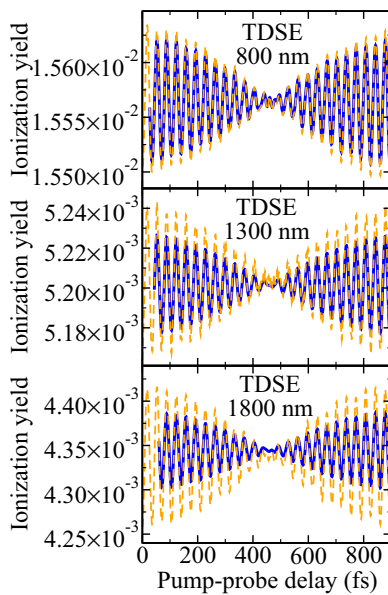


FIG. 7. As in Fig. 6, but for a less intense ten-cycle 4×10^{13} W/cm 2 probe pulse and showing only the TDSE ionization yields.

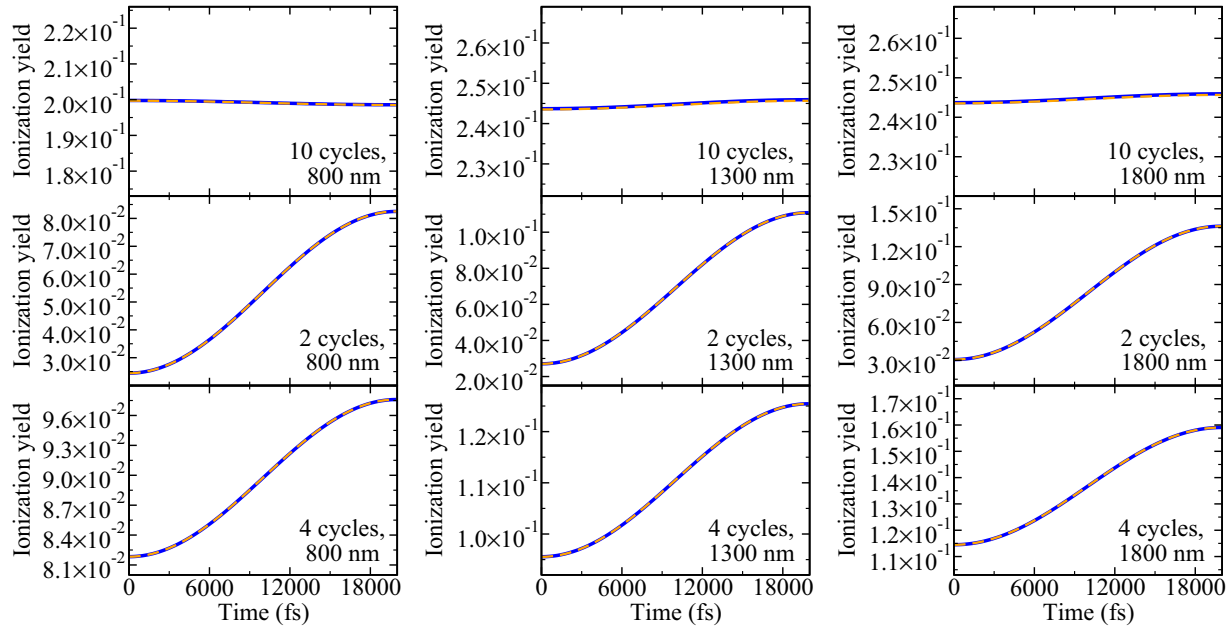


FIG. 8. Ionization yield for $I = 10^{14}$ W/cm² pulses (number of cycles and wavelength are given inside the graphs) probing the tunneling wave packet. Shown are the full time-dependent solutions of Eq. (6) (solid blue lines) and the results within the sudden-ionization approximation, Eq. (7) (dashed orange lines).

corresponds to the density localized on the right side. If a single ten-cycle laser pulse is used to probe this wave packet, the ionization yield remains, however, almost constant during the tunneling process, as seen in the top row of Fig. 8. Due to the symmetry of the tunneling process, the ionization yield even stays perfectly constant for an ionization yield $Y(x)$ which is symmetric in x ($\leftrightarrow -x$). This reflects the way this wave packet tunnels according to Eq. (15). Figure 9 shows

snapshots of the time evolution of this wave packet. Instead of “moving through” the barrier, the probability density rather disappears on one side of the barrier and appears on the other. Thus, even what naively seems to be the perfect detector for imaging the tunneling process, a symmetric probe where the signal is larger when the probability density is located farther inside the tunneling barrier, yields only a constant signal during the tunneling process.

V. BREAKING THE SYMMETRY: IMAGING WITH AN ASYMMETRIC IONIZATION YIELD

In order to follow the tunneling wave packet, Eq. (15), it is necessary to break the symmetry of the ionization yield $Y(x)$ with respect to x . This is the case if, for an oriented molecule, the direction of the electric-field maximum with respect to the dipole moment (see Fig. 4) leads to significantly different ionization yields for the parallel and antiparallel orientations, which was demonstrated and discussed for the water molecule [26]. Figure 10 shows that for very short pulses of only $n_c = 2$ cycles, the TDSE ionization yields are indeed highly asymmetric, for example, $Y(x = 0.73 \text{ a.u.})/Y(x = -0.73 \text{ a.u.}) \approx 3.7$ (4.6, 5.1) for 800 (1300, 1800) nm and $I = 10^{14}$ W/cm². For $n_c = 4$ cycles, the ionization yields are still notably asymmetric, e.g., $Y(x = 0.73 \text{ a.u.})/Y(x = -0.73 \text{ a.u.}) \approx 1.2$ (1.4, 1.4) for 800 (1300, 1800) nm and $I = 10^{14}$ W/cm². The asymmetry is superimposed on the previously discussed enhancement of the ionization yield for smaller $|x|$. Note that this asymmetry is not described within standard (FC-)ADK, Eq. (3), since the binding energy $I_p(x)$ is perfectly symmetric with respect to x . (A corresponding extension including dipole effects in the weak-field limit has, however, been suggested in [33,34].)

The second and third rows of Fig. 8 show the time dependence of the total ionization yield for the $n_c = 2-4$ cycle

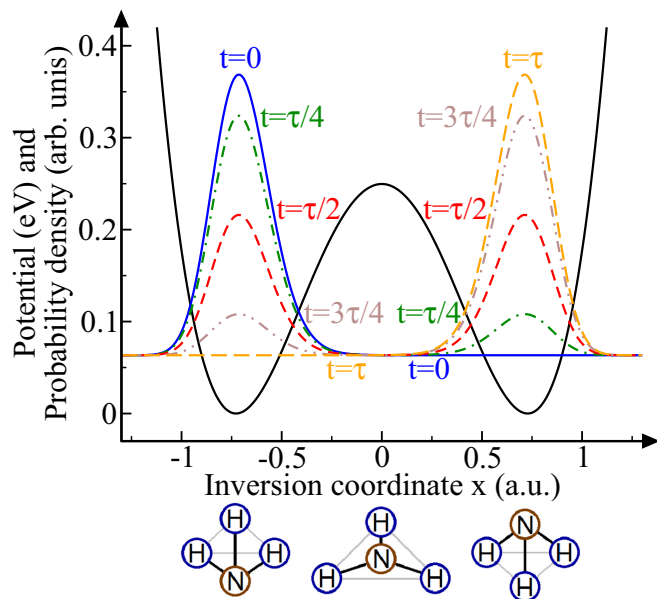


FIG. 9. Snapshots of the time evolution of a tunneling wave packet (solid blue line and dashed and dot-dashed lines) for $t = 0, \tau/4, \tau/2, 3\tau/4$ and τ in the ground-state potential of NH_3 (solid black line), where τ is the time required to tunnel from one well to the other completely, Eq. (14).

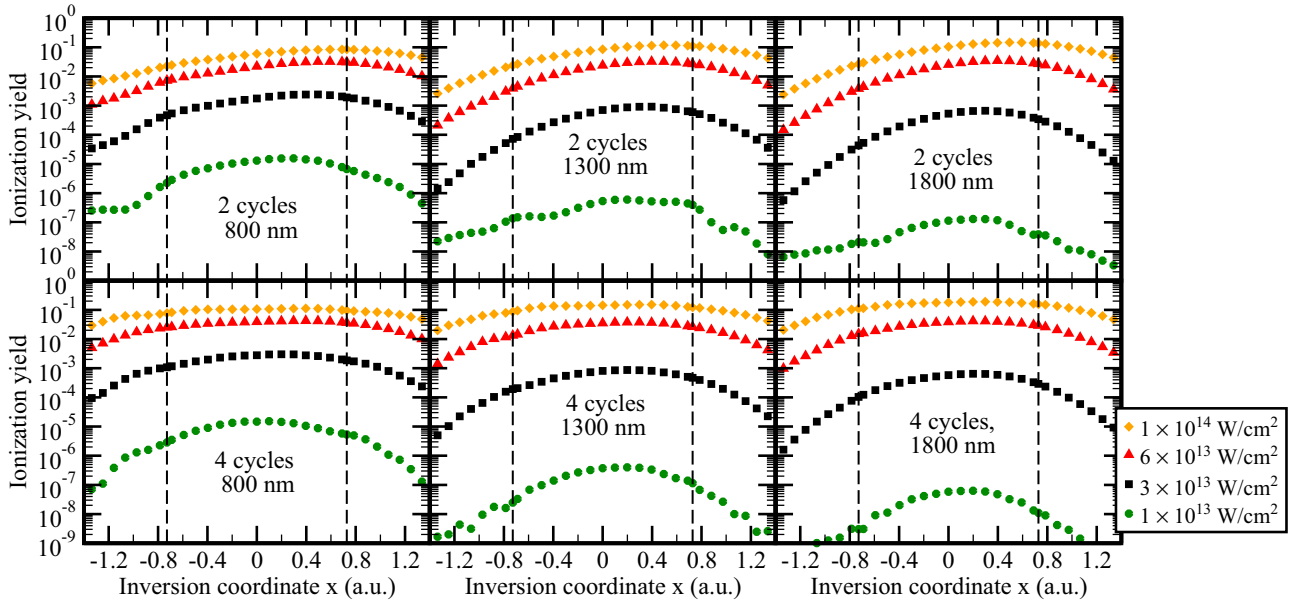


FIG. 10. As in Fig. 3, but for shorter two- and four-cycle pulses and using only TDSE ionization yields.

pulses from Fig. 10. As expected, the ionization yield strongly increases with time; thus, these pulses indeed allow for following the tunneling wave packet, Eq. (15), during the tunneling process. For these very short pulses, the sudden ionization approximation agrees perfectly with the full solution of Eq. (6).

An asymmetric wave packet in neutral NH_3 may also be created starting from the 50% $|0s\rangle$, 50% $|0a\rangle$ thermal equilibrium state by ionizing with an asymmetric ionization yield $Y(x)$ (see Fig. 11). We consider the *Lochfraß* pump-probe scheme previously discussed, except now using two two-cycle 10^{14} W/cm^2 pulses. In this case, the density matrix describing the ensemble is propagated within the sudden-ionization approximation since an independent propagation of $|0s\rangle$ and $|0a\rangle$ is not possible for an asymmetric ionization yield. However, as previously noted, the sudden-ionization approximation agrees perfectly with the solution of the TDSE for these very short pulses. Figure 12 shows the obtained probe-pulse ionization yields. The behavior of the probe-pulse ionization yield follows the expectation value $\langle x \rangle$ of the wave packet. The created asymmetry leads to a behavior similar to the tunneling wave packet in Fig. 8, but with a significantly smaller contrast since the asymmetry created by the pump pulse is smaller. Superimposed on the signal from tunneling is an oscillation similar to the signal for ten-cycle pulses (Fig. 6) due to the $|x|$ dependence of the ionization yield (Fig. 10). The contrast of this substructure depends on the $|x|$ dependence of the ionization yield on either side. For example, the very flat behavior of the ionization yield for $n_c = 2$ cycles, $\lambda = 800 \text{ nm}$, and $I = 10^{14} \text{ W/cm}^2$ (Fig. 10) leads to a rather small suboscillation of the ionization yield at the end of the tunneling process compared to its beginning (see Fig. 12).

Note that asymmetric ionization behavior may alternatively also be observed for longer pulses as asymmetry in the emission direction of the electrons and thus may be observed if the photoelectron spectra are recorded or it may be created by $\omega/2\omega$ pulses. Therefore, a number of possible experimental realizations of directly observing the tunneling process in ammonia exist.

VI. CONCLUSIONS

The geometry-dependent ionization behavior of ammonia has been studied by solving the TDSE within the single-determinant approximation. For ten-cycle pulses ADK qualitatively predicts the correct ionization yield, while

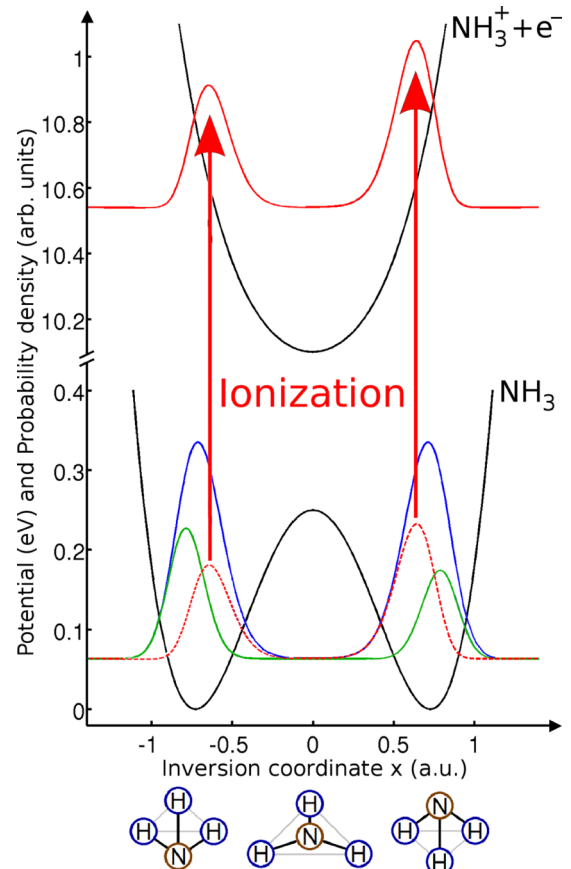


FIG. 11. As in Fig. 5, but for an asymmetric ionization yield.

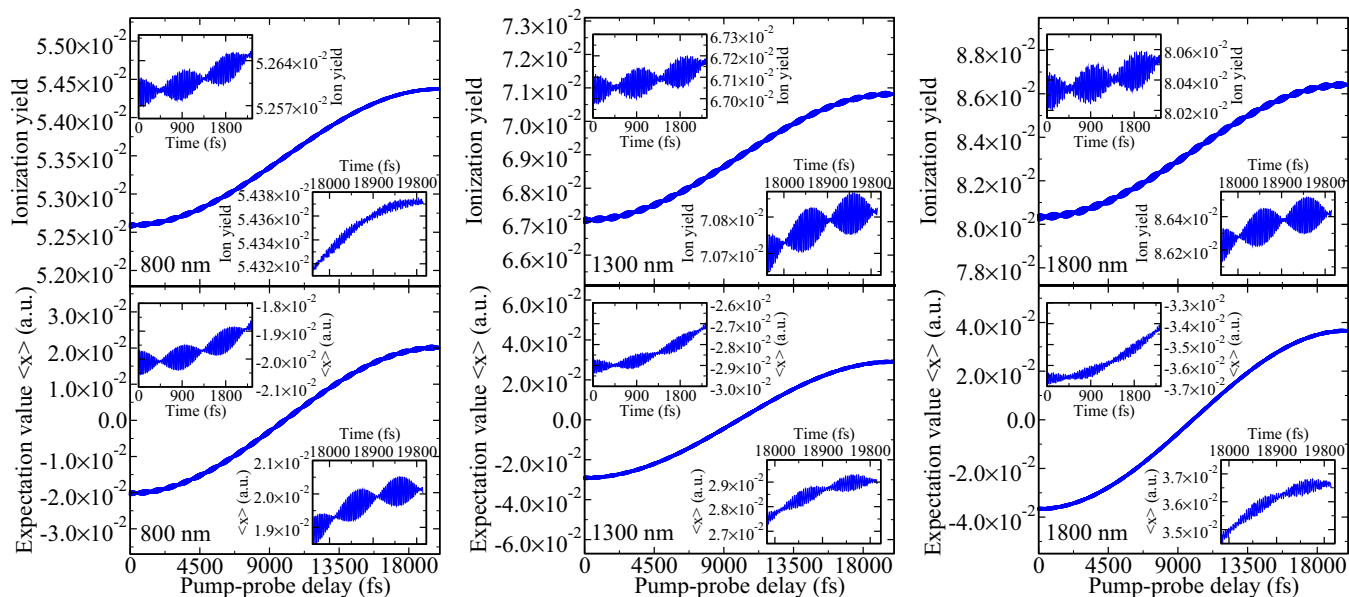


FIG. 12. Probe-pulse ionization yield as a function of the pump-probe delay for wavelengths 800, 1300, and 1800 nm. A two-cycle 10^{14} W/cm 2 pump pulse is followed by an identical two-cycle 10^{14} W/cm 2 probe pulse. Shown is the probe-pulse ionization yield obtained from the propagation of the density matrix (top) and the expectation value $\langle x \rangle$ of the created wave packet (bottom). The insets enlarge the signal at the beginning and end of the graph.

FC-ADK agrees with the TDSE almost quantitatively over the whole intensity range. However, both ADK and FC-ADK significantly overestimate the increase of the ionization yield with decreasing inversion coordinate $|x|$. Thus, while similar vibrational dynamics through *Lochfraß* can be observed using TDSE or (FC-)ADK ionization yields, the contrast of the oscillation of the ionization yield is much smaller for the TDSE ionization yield compared to (FC-)ADK. The contrast can, nevertheless, be improved using 1800 nm instead of 800 nm or a weaker probe pulse.

Furthermore, imaging of a tunneling wave packet has been discussed. While a detector leading to an increased ionization yield for wave packets close to the tunneling barrier may seem perfect to follow the tunneling process in real time, any geometry-dependent ionization yield symmetric in x leads to a perfectly constant signal. This can be understood by looking at how the probability density evolves during the tunneling process. It was shown that very short two- to four-cycle pulses break the symmetry of the geometry-dependent ionization yield with respect to x , allowing us to follow the tunneling wave packet in real time. Finally, *Lochfraß* using two two-cycle pulses shows both the behavior of the tunneling wave packet and the faster beating oscillations previously discussed for the longer ten-cycle pulses.

Clearly, an experimental measurement of the predictions made here would pave the way for future real-time movies of

quantum-mechanical nuclear motion in more than diatomic neutral molecules. The results show that FC-ADK may give a good estimate for laser parameters in order to observe *Lochfraß* also for other, especially more complex, molecules which undergo an equilibrium geometry change upon ionization, although the contrast may be overestimated. For oriented molecules, asymmetries in the ionization behavior allow for even more applications such as the real-time movie of the tunneling process discussed here. One may even be able to follow proton or heavy-atom tunneling in biologically relevant molecules [35–39], provided the ionization yield of the orbital dominating the strong-field ionization process (usually the HOMO) changes sufficiently as a function of the tunneling coordinate.

ACKNOWLEDGMENTS

We gratefully acknowledge many helpful discussions with and advice from P. Decleva as well as grants of computer time from CINECA. J.F. gratefully acknowledges a Ph.D. scholarship from the German National Academic Foundation (Studienstiftung des deutschen Volkes). We gratefully acknowledge financial support from the Deutsche Forschungsgemeinschaft (DFG) within Priority Programme 1840 QUTIF, the EU Initial Training Network (ITN) CORINF, and the European COST Action CM1204 (XLIC).

- [1] J. Itatani, J. Levesque, D. Zeidler, H. Niikura, H. Pépin, J. C. Kieffer, P. B. Corkum, and D. M. Villeneuve, *Nature (London)* **432**, 867 (2004).
- [2] M. Lein, *Phys. Rev. Lett.* **94**, 053004 (2005).
- [3] S. Baker, J. S. Robinson, C. A. Haworth, H. Teng, R. A. Smith, C. C. Chirilă, M. Lein, J. W. G. Tisch, and J. P. Marangos, *Science* **312**, 424 (2006).
- [4] J. P. Farrell, S. Petretti, J. Förster, B. K. McFarland, L. S. Spector, Y. V. Vanne, P. Decleva, P. H. Bucksbaum, A. Saenz, and M. Gühr, *Phys. Rev. Lett.* **107**, 083001 (2011).
- [5] P. Kraus and H. Wörner, *ChemPhysChem* **14**, 1445 (2013).
- [6] J. Förster and A. Saenz, *ChemPhysChem* **14**, 1438 (2013).
- [7] H. J. Wörner, J. B. Bertrand, D. V. Kartashov, P. B. Corkum, and D. M. Villeneuve, *Nature (London)* **466**, 604 (2010).

- [8] H. J. Wörner, J. B. Bertrand, B. Fabre, J. Higuette, H. Ruf, A. Dubrouil, S. Patchkovskii, M. Spanner, Y. Mairesse, V. Blanchet *et al.*, *Science* **334**, 208 (2011).
- [9] M. Meckel, D. Comtois, D. Zeidler, A. Staudte, D. Pavičić, H. C. Bandulet, H. Pépin, J. C. Kieffer, R. Dörner, D. M. Villeneuve *et al.*, *Science* **320**, 1478 (2008).
- [10] S. Petretti, Y. V. Vanne, A. Saenz, A. Castro, and P. Decleva, *Phys. Rev. Lett.* **104**, 223001 (2010).
- [11] X. Urbain, B. Fabre, E. M. Staiacu-Casagrande, N. de Ruelle, V. M. Andrianarijaona, J. Jureta, J. H. Posthumus, A. Saenz, E. Baldit, and C. Cornaggia, *Phys. Rev. Lett.* **92**, 163004 (2004).
- [12] A. Saenz, *J. Phys. B* **33**, 4365 (2000).
- [13] A. M. Perelomov, V. S. Popov, and M. V. Terent'ev, *Sov. Phys. JETP* **23**, 924 (1966).
- [14] M. V. Ammosov, N. B. Delone, and V. P. Krainov, *Sov. Phys. JETP* **64**, 1191 (1986).
- [15] F. A. Ilkov, J. E. Decker, and S. L. Chin, *J. Phys. B* **25**, 4005 (1992).
- [16] M. Awasthi and A. Saenz, *J. Phys. B* **39**, S389 (2006).
- [17] Y. V. Vanne and A. Saenz, *Phys. Rev. A* **80**, 053422 (2009).
- [18] J. Förster, Y. V. Vanne, and A. Saenz, *Phys. Rev. A* **90**, 053424 (2014).
- [19] E. Goll, G. Wunner, and A. Saenz, *Phys. Rev. Lett.* **97**, 103003 (2006).
- [20] T. Ergler, B. Feuerstein, A. Rudenko, K. Zrost, C. D. Schröter, R. Moshhammer, and J. Ullrich, *Phys. Rev. Lett.* **97**, 103004 (2006).
- [21] L. Fang and G. N. Gibson, *Phys. Rev. Lett.* **100**, 103003 (2008).
- [22] L. Fang and G. N. Gibson, *Phys. Rev. A* **78**, 051402(R) (2008).
- [23] M. Spanner, S. Patchkovskii, E. Frumker, and P. Corkum, *Phys. Rev. Lett.* **109**, 113001 (2012).
- [24] E. Frumker, C. T. Hebeisen, N. Kajumba, J. B. Bertrand, H. J. Wörner, M. Spanner, D. M. Villeneuve, A. Naumov, and P. B. Corkum, *Phys. Rev. Lett.* **109**, 113901 (2012).
- [25] M. Awasthi, Y. V. Vanne, A. Saenz, A. Castro, and P. Decleva, *Phys. Rev. A* **77**, 063403 (2008).
- [26] S. Petretti, A. Saenz, A. Castro, and P. Decleva, *Chem. Phys.* **414**, 45 (2013).
- [27] Software for Chemistry & Materials, Amsterdam density functional, <https://www.scm.com>
- [28] N. Aquino, G. Campoy, and H. Yee-Madeira, *Chem. Phys. Lett.* **296**, 111 (1998).
- [29] In contrast to Ref. [28] we choose a Hermitian ordering for the kinetic energy operator. As found in Sec. IV A of Ref. [30], the eigenenergies are practically independent of the choice of where $\mu(x)$ enters the Hamiltonian.
- [30] J. Förster, A. Saenz, and U. Wolff, *Phys. Rev. E* **86**, 016701 (2012).
- [31] V. Spirko, *J. Mol. Spectrosc.* **101**, 30 (1983).
- [32] J. Gordon, H. Zeiger, and C. Townes, *Phys. Rev.* **95**, 282 (1954).
- [33] O. I. Tolstikhin, T. Morishita, and L. B. Madsen, *Phys. Rev. A* **84**, 053423 (2011).
- [34] O. I. Tolstikhin, L. B. Madsen, and T. Morishita, *Phys. Rev. A* **89**, 013421 (2014).
- [35] P.-O. Löwdin, *Rev. Mod. Phys.* **35**, 724 (1963).
- [36] L. Masgrau, A. Roujeinikova, L. O. Johannissen, P. Hothi, J. Basran, K. E. Ranaghan, A. J. Mulholland, M. J. Sutcliffe, N. S. Scrutton, and D. Leys, *Science* **312**, 237 (2006).
- [37] O. M. Gonzalez-James, X. Zhang, A. Datta, D. A. Hrovat, W. T. Borden, and D. A. Singleton, *J. Am. Chem. Soc.* **132**, 12548 (2010).
- [38] R. K. Allemann and N. S. Scrutton (eds.), *Quantum Tunnelling in Enzyme-Catalysed Reactions* (RSC Publishing, Cambridge, 2009).
- [39] M. Arndt, T. Juffmann, and V. Vedral, *HFSP J.* **3**, 386 (2009).